PAPER

Check for updates

Plasmon photocatalytic CO$_2$ reduction reactions over Au particles on various substrates†

Kai Wang[a,b] and Tao He [ID] *[a,b]

Surface plasmonic effects have been widely used in photocatalytic reactions like CO$_2$ conversion in the past decades. However, owing to the significant controversy in the physical processes of plasmon photocatalytic reactions and difficulty in realizing CO$_2$ reduction, the influence mechanism of the plasmon effect on the CO$_2$ photoreduction is still under debate. In this study, Au particles deposited on various substrates were employed to acquire insights into the plasmon photocatalytic CO$_2$ reduction, including SiO$_2$, n-Si, p-Si, TiO$_2$–SiO$_2$, TiO$_2$-n-Si, and TiO$_2$-p-Si. It was found that the plasmon resonant enhancement (PRE) effect of Au–SiO$_2$ caused by the Au plasmon was stronger than that of Au–TiO$_2$–SiO$_2$ and Au-n-Si (Au-p-Si) in the visible-light range, while it was weaker for Au-n-Si (Au-p-Si) samples than Au–TiO$_2$-n-Si (Au–TiO$_2$-p-Si). The simulation results agree with the experimental conclusions. The photocatalytic results indicated that the catalytic activity of Au-n-Si (Au-p-Si) samples was lower than that of Au–TiO$_2$-n-Si (Au–TiO$_2$-p-Si), and Au–SiO$_2$ was lower than Au–TiO$_2$-SiO$_2$ and Au-n-Si (Au-p-Si) samples, suggesting that the direct electron transfer (DET) mechanism was dominant here compared with the PRE mechanism.

1. Introduction

The photocatalytic conversion of CO$_2$ into value-added chemicals has attracted great interest recently. Since CO$_2$ reduction with H$_2$O was reported for the first time in the late 1970's,[1,2] plenty of studies have been reported, including catalyst materials, the utilization of solar energy, and improvement of catalytic activity of CO$_2$ photoreduction.[3–12] Although great advances have been made hitherto, there are still two major challenges,[13] *i.e.*, the lack of appropriate visible light-responsive materials and low photocatalytic activity. The first one is mainly because many high-catalytic-performance materials (such as TiO$_2$, ZnO, and ZnS) usually have a wide bandgap and show absorption responses in the near UV range. The second is closely related to the severe recombination of photoexcited electrons and holes, especially in the narrow-bandgap catalysts (such as Fe$_2$O$_3$, CdS, Cu$_2$O, and Si). Thus, it is pressing and significantly important to construct photocatalytic systems for CO$_2$ reduction that can efficiently use visible-light energy. For

instance, heterojunctions have been widely used for this, such as Cu$_2$O/ZnO,[14] α-Fe$_2$O$_3$/CoFe$_2$O$_4$,[15] and α-Fe$_2$O$_3$/ZnO.[16]

The rapid development of surface plasmon resonance (SPR) has provided a new opportunity to overcome the above limit of the photocatalytic CO$_2$ reduction reaction (CO$_2$RR).[17–21] The localized surface plasmon resonance (LSPR) induced by metal particles (such as Au, Ag, and Cu) mainly has two attenuation pathways:[22] the local electromagnetic field enhancement (LEFE) induced by radiative attenuation and hot electrons emerging from non-radiative attenuation. The LSPR possesses the advantages of enhanced absorption of incident light and the broadened response band of sunlight. The plasmonic systems usually include pure metal nanoparticles, metal–insulator structures, and metal–semiconductor heterostructures. The improved photocatalytic activity by metal nanoparticles and metal–insulator structures is mainly due to the metallic LEFE. For the metal–semiconductor heterostructures, besides the LEFE effect, the Schottky junction and fast charge-transport lane at metal/semiconductor interface work together to promote the charge transfer and suppress the electron–hole recombination, which makes it confusing if the charge carriers and reaction sites originate from the metal or semiconductor in the photocatalytic CO$_2$RR.

The mechanism of enhanced catalytic activity caused by the LSPR still remains unclear or controversial hitherto. The reported mechanisms are LEFE,[17,23,24] direct electron transfer (DET),[25–27] resonant energy transfer (RET),[22,28,29] local heating effect,[30,31] exciton quenching,[32] electron trapping center,[33] and direct charge generation.[34] The major controversy involves the LEFE, DET and RET. SPR-mediated radiative LEFE can

[a]CAS Key Laboratory of Nanosystem and Hierarchical Fabrication, National Center for Nanoscience and Technology, Beijing 100190, China. E-mail: het@nanoctr.cn
[b]University of Chinese Academy of Sciences, Beijing 100049, China

†Electronic supplementary information (ESI) available: Size distribution of Au particles on various substrates, optical refractive index and extinction coefficient of different substrates, optical properties of TiO$_2$, Au and Au/TiO$_2$ on different substrates, UV-vis absorption spectrum of R6G, photocurrent, surface temperature, alignment of energy levels for different samples, including Fig. S1–S10. See DOI: https://doi.org/10.1039/d3nr02543h

directly cause the occurrence of the photocatalytic reactions due to the strong oscillation of free electrons in the metal of metal–insulator structures, such as Au/SiO_2 [35] and Au/Al_2O_3 systems.[36] When the LEFE-induced energy is higher than the bandgap value of a semiconductor in the metal–semiconductor heterostructures, the LEFE can also contribute to the generation of electron–hole pairs in the semiconductor, such as Au–TiO_2, Ag–TiO_2, Au–CdS, Au–Cu_2O, and Au–Si.[37–39]

In the DET process, LSPR-excited hot electrons transfer from the metal to the conduction band of the semiconductor, and then take part in the photocatalytic reaction. Hence, there is no DET effect between the reactants and pure metal nanoparticles or metal–insulator structures. However, the RET-induced photocatalytic reaction is feasible for pure metal particles or metal–insulator structures. In a nonradiative RET process, the energy generated by relaxation of the localized surface plasmon dipole is transmitted to the semiconductor, leading to the formation of electron–hole pairs in the semiconductor of the metal–semiconductor heterostructure.

Since the energy source of the photocatalytic CO_2RR following the LEFE and RET mechanisms is the same (*i.e.*, electromagnetic energy excited by LSPR on the metal surface) and both can stimulate the electron–hole pairs in the semiconductor of metal–semiconductor heterostructures, here they are classified as one in order to be different from the DET mechanism, which is denoted as plasmon resonant enhancement (PRE). Thus, the main objective of this work is to distinguish the PRE mechanism from DET and analyze the pertinent role in various catalytic systems.

Herein, Au was chosen as the metallic material to excite the LSPR because of its high stability, strong antioxidant capacity and good optical properties of plasmon, which was deposited on various substrates by physical method due to the high precision and uniform size distribution compared with the chemical method. To make the PRE mechanism dominant and block the DET effect, a metal–insulator structure was employed, such as Au–SiO_2. Conversely, the structures with a Schottky junction like Au–TiO_2 and Au-n-Si were adopted because the metal–semiconductor heterojunctions facilitate the DET process. The barrier height of Au–TiO_2 [25,40] and Au-n-Si[41] is 1.0 and 0.82 eV, respectively. Moreover, the wide-bandgap TiO_2 favors the suppression of the electron–hole recombination compared with the low-bandgap Si. Au–TiO_2 shows better performance of charge separation and transfer than Au–Si, exhibiting a stronger DET effect. For comparison, both n-type silicon (n-Si) and p-type silicon (p-Si) substrates were employed. Accordingly, the plasmon effect of various systems (Au–SiO_2, Au–TiO_2–SiO_2, Au-n-Si, Au-p-Si, Au–TiO_2-n-Si and Au–TiO_2-p-Si) and the resultant influence on the photocatalytic CO_2RR were thoroughly studied.

2. Experimental section

2.1 Sample preparation

Three types of wafers were used as substrates to prepare the samples, *i.e.*, n-Si (⟨100⟩), p-Si (⟨100⟩) and 1 μm thick SiO_2 on Si. The wafers were first cut into small shards (4.5 cm × 4.5 cm) and washed consecutively under sonication for 10 min in acetone and isopropanol, followed by thorough rinsing with Milli-Q water. The obtained shards were heated for 10 min in Piranha solution (98% H_2SO_4 : H_2O_2, 5 : 1, v/v) at 70 °C (*Treated with Caution*), followed by treatment with RCA protocol, *i.e.*, first in a mixture of H_2O : NH_4OH (25%) : H_2O_2 (30%) (7 : 2 : 1, v/v) at 70 °C for 10 min, and then in a mixture of H_2O (32%) : HCl : H_2O_2 (30%) (7 : 2 : 1, v/v) at 70 °C for 10 min. After rinsing with Milli-Q water, a 5 nm thick Au thin film was deposited onto the surface of the obtained shards using an E-beam evaporator (OHMIKER-50B) with a deposition rate of 0.01 nm s^{-1}. In addition, a 5 nm thick Au thin film was deposited onto a 100 nm thick TiO_2 film, which had been pre-deposited onto the aforementioned three types of substrates by the above E-beam evaporator.

2.2 Instrumentation

The topographies of the obtained samples were observed by atomic force microscope (AFM, ICON2-SYS). The optical properties were studied by a spectroscopic ellipsometer (SE 850 DUV). Raman spectra were collected within the range of 550–1800 cm^{-1} excited by a 633 nm laser on a micro-Raman spectrometer (Renishaw inVia plus), with one drop of 10^{-6} mol L^{-1} Rhodamine 6G (R6G) dispersed on the surface. The transient photocurrent was measured using a three-electrode system by an electrochemical workstation (Zahner-IM6) with a cutoff filter (420 nm).

2.3 Photocatalytic performance

The photocatalytic CO_2RR was carried out in a quartz-tube reactor (500 mL) with a 500 W spherical Xe lamp (Philips, Belgium) as the light source and the wavelength longer than 290 nm. The sample size was 4.5 cm × 4.5 cm, with the upper surface perpendicular to the light beam. Pure CO_2 gas (≥99.999%) was continuously purged into the reactor for 1 h (0.3 L min^{-1}) to remove the air and other impurity gases before the photoreduction experiments. The quartz tube was sealed by a rubber stopper. Then, 2 mL of Milli-Q water was injected into the reactor and the light was switched on for photocatalysis. The products were analyzed every 2 h using a gas chromatography apparatus (GC7890F, Shanghai Techcomp Instrument Co., Ltd).

3. Results

Both Au and TiO_2 have been deposited onto various substrates by E-beam evaporation with a thickness of 5 and 100 nm, respectively. As shown in Fig. 1(a, e and i), the surface of the SiO_2, n-Si and p-Si substrates is quite smooth with a roughness of ~0.1 nm. When TiO_2 is coated on the three substrates, the roughness becomes 0.9 nm (Fig. 1(c, g and k)). The surfaces with Au nanomaterials grew on SiO_2, n-Si and p-Si, or on the TiO_2 surface atop SiO_2, n-Si and p-Si, and all showed a roughness of around 1.2 nm. According to the results of size distri-
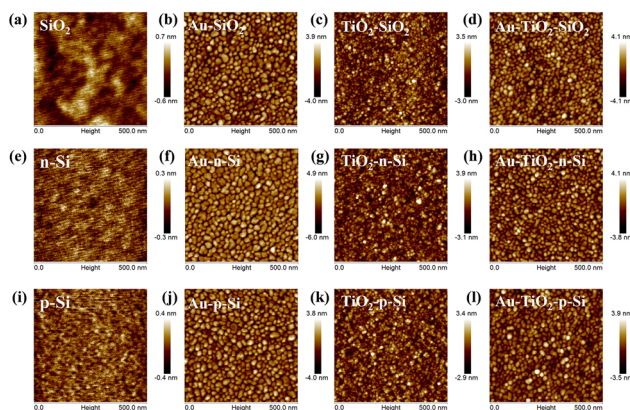
Fig. 1 AFM morphology of all samples for (a) SiO$_2$, (b) Au–SiO$_2$, (c) TiO$_2$–SiO$_2$, (d) Au–TiO$_2$–SiO$_2$, (e) n-Si, (f) Au-n-Si, (g) TiO$_2$-n-Si, (h) Au–TiO$_2$-n-Si, (i) p-Si, (j) Au-p-Si, (k) TiO$_2$-p-Si, and (l) Au–TiO$_2$-p-Si.

Fig. 2 Refractive index of Au particles for different samples. (a) Au–SiO$_2$, Au-n-Si and Au-p-Si, (b) Au–SiO$_2$ and Au–TiO$_2$–SiO$_2$, (c) Au-n-Si and Au–TiO$_2$-n-Si, and (d) Au-p-Si and Au–TiO$_2$-p-Si.

Fig. 3 Extinction coefficient of Au particles for different samples. (a) Au–SiO$_2$, Au-n-Si and Au-p-Si, (b) Au–SiO$_2$ and Au–TiO$_2$–SiO$_2$, (c) Au-n-Si and Au–TiO$_2$-n-Si, and (d) Au-p-Si and Au–TiO$_2$-p-Si.

bution (Fig. S1†) and particle size statistics (Fig. S2†), the average size of all Au particles is 20 ± 5 nm. Thus, various substrates have almost no impact on the morphology of Au.

The spectroscopic ellipsometer has been used to study the optical properties of all samples. The refractive index of SiO$_2$ is between 1.45–1.50, and its extinction coefficient is zero in the full spectrum due to the wide bandgap of 9 eV (Fig. S3(a)†). The n-Si and p-Si substrates exhibit the same optical properties as intrinsic Si (Fig. S3(b and c)†), which has an extinction coefficient of nearly zero in the visible-light range, and thus exhibits almost no absorption of incident light. However, the extinction coefficient of n-Si (p-Si) clearly increases in the UV range, corresponding to a bandgap of 3.1 eV, which is caused by the inter-band transition of n-Si (p-Si) at high energy levels. Accordingly, a peak appears in the UV region for the refractive index of n-Si (p-Si). Similarly, the bandgap of the TiO$_2$ film on all substrates of SiO$_2$, n-Si and p-Si is determined to be ~3.3 eV (Fig. S4†), consistent with the literature values.[42]

It seems that the three samples of Au–SiO$_2$, Au-n-Si and Au-p-Si have the same dispersion dn/dλ according to the respective refractive index of Au particles (Fig. 2(a)). The refractive index of Au–SiO$_2$ is larger than that of Au-n-Si and Au-p-Si, which may cause deflection of incident light in the Au medium for Au–SiO$_2$, resulting in total reflection and thereby facilitating the plasmon excitation. Hence, the plasmon effect of the Au particles on the SiO$_2$ substrate is stronger than that of n-Si and p-Si. Similarly, the optical performance of Au in Au–SiO$_2$ is superior to that in Au–TiO$_2$–SiO$_2$ (Fig. 2(b)). These can be verified by the extinction coefficient of Au in the different samples. The Au particles on the SiO$_2$ substrate have the same extinction peak position (~600 nm) as that on the n-Si and p-Si substrates (Fig. 3(a)), while the spectral bandwidth of Au–SiO$_2$ is narrower than that of Au-n-Si and Au-p-Si. This means the Au particles on the SiO$_2$ substrate exhibit a longer plasmon dephasing time, which is defined as $T = 2\hbar/\Gamma$, where Γ is the full width at half maximum (FWHM).[43–45] The dephasing time of the Au particles on the SiO$_2$ substrate is 2.3
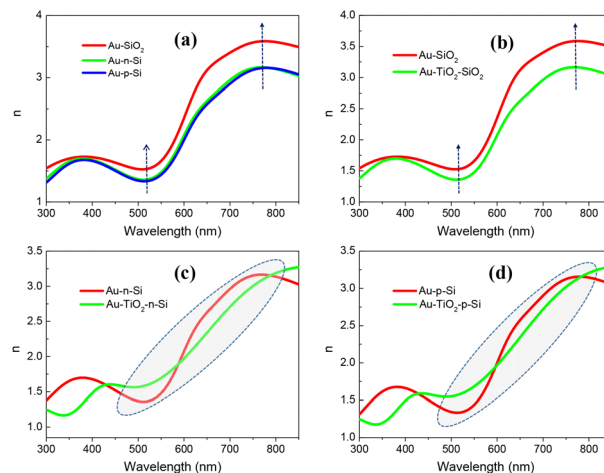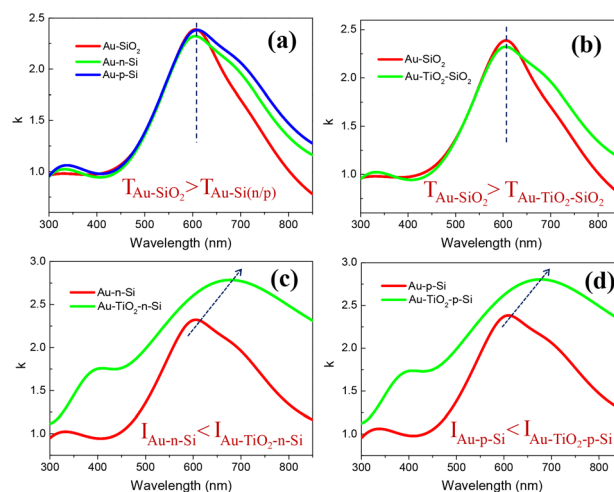
fs, which is longer than that of ~1.9 fs for Au-n-Si and Au-p-Si, leading to a stronger plasmon effect. In addition, the dephasing time of the Au–SiO$_2$ sample is longer than that for Au–TiO$_2$–SiO$_2$ (~1.9 fs), implying that the introduction of the TiO$_2$ interlayer can restrain the plasmon intensity.

According to Fig. 2(c–d) and 3(c–d), the Au particles on the n-Si and p-Si substrates exhibit the same optical properties. Meanwhile, Au–TiO$_2$-n-Si has the same optical properties as Au–TiO$_2$-p-Si. The refractive index spectrum of the Au particles for Au-n-Si overlaps with that of the Au–TiO$_2$-n-Si sample (Fig. 2(c)) in the UV-visible light range. The same phenomenon is observed between the Au-p-Si and Au–TiO$_2$-p-Si samples (Fig. 2(d)). Thus, it is difficult to probe the plasmon characteristics in terms of the refractive index and dispersion behavior. However, the extinction spectra of the Au particles on the n-Si

and p-Si substrates are much lower than the counterpart samples of Au–TiO$_2$-n-Si and Au–TiO$_2$-p-Si (Fig. 3(c and d)), indicating that Au-n-Si and Au-p-Si can exhibit stronger plasmon effects. Interestingly, all of the samples with the TiO$_2$ film but without Au particles exhibit almost the same optical properties (Fig. S4†). Meanwhile, big differences can be observed in the optical properties among the samples when the Au particles are deposited on the surface of a narrow-bandgap semiconductor (n-Si & p-Si), a wide-bandgap semiconductor (TiO$_2$), and a dielectric material (SiO$_2$) (Fig. 2, 3 & Fig. S5, S6†), which is related to the plasmon effect of the Au particles and the interaction between the Au particles and the substrate. In addition, it should be noted that the size of the Au particles on TiO$_2$ seems to slightly decrease compared to those on the SiO$_2$ substrate (Fig. S2†). In this case, the redshift in the extinction spectra once the TiO$_2$ layer is deposited onto the Si substrates (Fig. 3(c and d)) is probably related to the Au/TiO$_2$ heterojunction possibly elongating the distance of charge transfer and preventing the recombination of hot carriers, leading to an increased plasmon oscillation period.

Surface enhanced Raman scattering (SERS) is used to further study the plasmon effect of Au particles on various substrates using R6G as the probe. The R6G molecule shows an absorption peak at 527 nm (Fig. S7†), and has a gap of 2.35 eV between HOMO and LOMO.[46] Thus, a 633 nm laser is employed as the excitation source so as to avoid the influence of R6G absorption. The SERS effect cannot be observed for the samples without Au particles, while the samples with Au exhibit typical Raman signals of R6G at 1362 cm^{-1} (C–C and C–N stretching mode) and 1510 cm^{-1} (C–C stretching mode)[47] (Fig. 4). Au–SiO$_2$ shows a larger Raman enhancement factor than Au–TiO$_2$–SiO$_2$ because it has higher Raman intensity, whereas Au-n-Si (Au-p-Si) has lower enhancement than Au–TiO$_2$-n-Si (Au–TiO$_2$-p-Si). This means that the introduction of the TiO$_2$ interlayer leads to the opposite impact on the plasmon effect for the same substrate, i.e., Au–SiO$_2$ is stronger than Au–TiO$_2$–SiO$_2$ and Au-n-Si (Au-p-Si) is weaker than Au–TiO$_2$-n-Si (Au–TiO$_2$-p-Si). Similarly, Au–SiO$_2$ shows a stronger plasmon effect than Au-n-Si (Au-p-Si). All of these Raman results are consistent with the above optical ones.

In addition, the reflection coefficient of Au and Au/TiO$_2$ on different substrates are studied to explore the plasmon effect, which were measured by a home-built optical system.[48] For the SiO$_2$ substrate, the reflection coefficient of Au is lower than that of Au/TiO$_2$ in the visible-light region, but higher than that of Au/TiO$_2$ in the UV region. This is mainly due to the interband transition of TiO$_2$ (Fig. 5(a)). So, the absorption of Au–SiO$_2$ is stronger than Au–TiO$_2$–SiO$_2$ in the visible range, resulting in a higher potential to collect electromagnetic waves, and thus generate a larger local field. For the n-Si and p-Si substrates, the reflection coefficient of Au particles is higher than that of Au/TiO$_2$ in the full spectrum range, especially in the visible range (Fig. 5(b and c)). The slightly larger reflection of the Au coefficient on n-Si and p-Si in the UV region may be caused by the interband transitions from the ground state to the higher excited states of Si. Accordingly, Au–TiO$_2$-n-Si (Au–
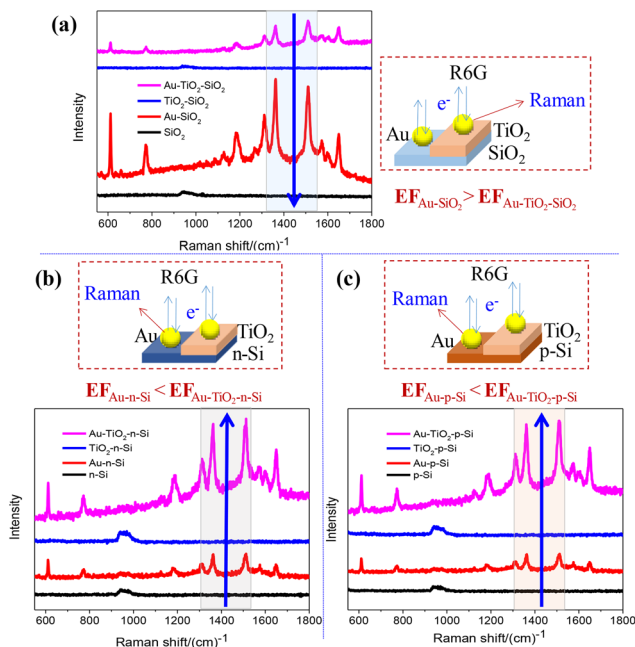

Fig. 4 Raman spectra of R6G for different samples. (a) Au and Au/TiO$_2$ on SiO$_2$, (b) Au and Au/TiO$_2$ on n-Si, and (c) Au and Au/TiO$_2$ on p-Si.
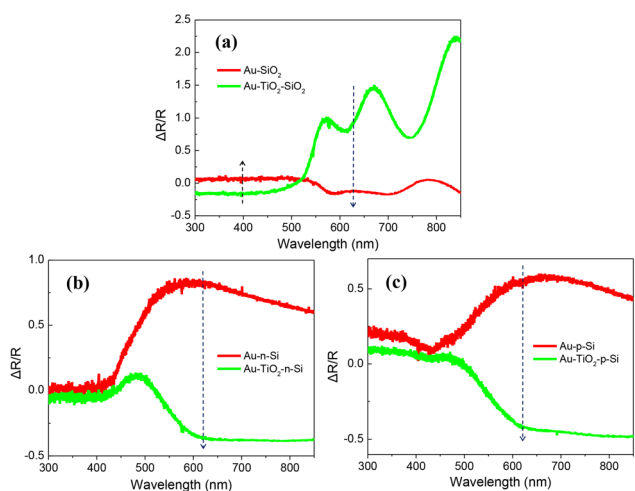

Fig. 5 Reflection coefficient of Au and Au/TiO$_2$ on different substrates of (a) Au–SiO$_2$ and Au–TiO$_2$–SiO$_2$, (b) Au-n-Si and Au–TiO$_2$-n-Si, and (c) Au-p-Si and Au–TiO$_2$-p-Si.

TiO$_2$-p-Si) has a stronger binding ability to incident light than Au-n-Si (Au-p-Si), which is in favor of the excitation of a plasmon and production of a larger local field. Therefore, the results of reflection agree with those of both ellipsometry and Raman characterizations.

The above phenomena can also be verified by the energy loss function (ELF) of the plasmon,[49] which is defined by Im $\{-1/(1 + \varepsilon)\} = \varepsilon_2/[(1 + \varepsilon_1)^2 + \varepsilon_2^2]$, where ε is the dielectric constant with ε_1 and ε_2 as the real and imaginary parts, respectively. The peak position can illustrate the energy loss behavior

induced by electrons after excitation. The ELF of Au on SiO_2 is lower than that on n-Si and p-Si (Fig. 6(a)), indicating the stronger excitation of plasmon for Au–SiO_2 and thereby greater plasmon effect. In addition, the ELF of Au–SiO_2 is lower than that on Au–TiO_2–SiO_2 (Fig. 6(b)), implying that the plasmon effect of Au–SiO_2 is stronger than that of Au–TiO_2–SiO_2. The ELF of Au-n-Si (Au-p-Si) is higher than that of Au–TiO_2-n-Si (Au–TiO_2-p-Si) in the visible-light range (Fig. 6(c and d)). Thus, Au–TiO_2-n-Si (Au–TiO_2-p-Si) exhibits superior plasmon characteristics to Au-n-Si (Au-p-Si). In brief, all the results from various characterizations suggest that Au–SiO_2 shows stronger plasmon effect than Au–TiO_2–SiO_2, Au-n-Si and Au-p-Si, and Au-n-Si (Au-p-Si) is inferior to Au–TiO_2-n-Si (Au–TiO_2-p-Si).

All the samples are investigated by FDTD simulations, so as to verify the above experimental results. The Au particles for all of the samples have an average size of about 20 nm based on the AFM images, and have the shape of an approximate ellipsoid with the long and short axes of 24 and 16 nm, respectively. The thickness of the TiO_2 layer is 100 nm. The optical parameters of all of the materials used in the simulation are those obtained from the ellipsometry characterizations. The light source is in the visible range (420–760 nm). The distribution of the electric field intensity at the interface of Au and the medium below it is shown in Fig. 7. According to the color scale, Au–SiO_2 has a higher electric field intensity than Au–TiO_2–SiO_2, while Au-n-Si (Au-p-Si) is lower than Au–TiO_2-n-Si (Au–TiO_2-p-Si). The maximum enhancement factor $|E_{max}|/|E_0|$ of Au–SiO_2, Au–TiO_2–SiO_2, Au-n-Si (Au-p-Si) and Au–TiO_2-n-Si (Au–TiO_2-p-Si) is 3.31, 1.96, 0.86 and 2.47, respectively. Thus, Au–SiO_2 has the highest $|E_{max}|/|E_0|$, facilitating stronger excitation of plasmon compared with Au–TiO_2–SiO_2 and Au-n-Si (Au-p-Si). Au-n-Si (Au-p-Si) is more likely to suppress the excitation of the plasmon compared with Au–TiO_2-n-Si (Au–TiO_2-p-Si), i.e., leading to a weaker plasmon effect. Hence, the simulation results are consistent with all of the above experimental results. Accordingly, the difference in the plasmon effect
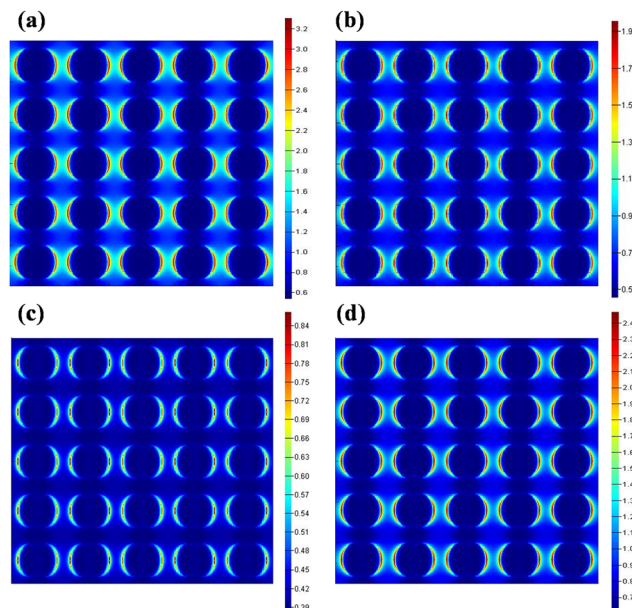

Fig. 7 Distribution of the electric field intensity at the interface of Au and the medium below it under visible-light illumination. (a) Au–SiO_2, (b) Au–TiO_2–SiO_2, (c) Au-n-Si (Au-p-Si), and (d) Au–TiO_2-n-Si (Au–TiO_2-p-Si).

among various samples can be used to elucidate the photocatalytic results.

The photocatalytic performance is studied using a filter with a cut-off wavelength of 420 nm for all of the samples. The blank samples like SiO_2, n-Si and p-Si have no catalytic activity under visible-light irradiation (Fig. 8), which agrees with the previous optical results. Once TiO_2 is coated on these three substrates, a small amount of CO and CH_4 is observed due to the existence of oxygen vacancies in TiO_2.[17] Upon the introduction of Au particles, the CO yield increases almost linearly with illumination time for all of the samples containing Au or Au/TiO_2, and the CH_4 yield also clearly increases. The production of CH_4 may proceed through the carbene path with the as-generated CO as the intermediate.[50] Since the value of the CH_4 yield is close to the detection limit in some sense, only CO production is used to study the catalytic activity and pertinent mechanism. For the SiO_2 substrate, the CO yield is 2.09 and 3.18 μmol h^{-1} cm^2 for Au–SiO_2 and Au–TiO_2–SiO_2, respectively (Fig. 8(a and b)), i.e., the catalytic activity of Au–SiO_2 is lower than that of Au–TiO_2–SiO_2. For the n-Si (p-Si) substrate, the respective CO yield is 2.50 (2.31) and 2.78 (2.58) μmol h^{-1} cm^2 for Au-n-Si (Au-p-Si) and Au–TiO_2-n-Si (Au–TiO_2-p-Si) (Fig. 8(c–f)). Thus, the catalytic activity of Au-n-Si (Au-p-Si) is lower than that of Au–TiO_2-n-Si (Au–TiO_2-p-Si).

To verify the phenomena that Au–TiO_2-n-Si (Au–TiO_2-p-Si) exhibits higher catalytic activity than Au-n-Si (Au-p-Si), transient photocurrent is used to study the electron transfer behavior (Fig. S8†). Because the photocatalytic performances for the samples based on the n-Si and p-Si substrates are quite similar, only the samples on n-Si are reported here. Almost no photocurrent can be observed for TiO_2-n-Si due to the wide-bandgap
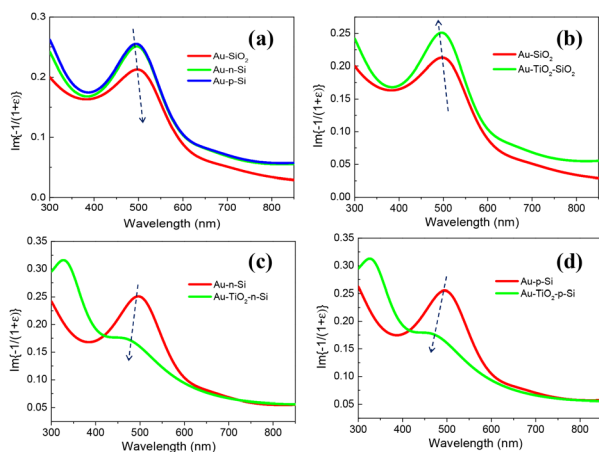

Fig. 6 Energy loss function of Au particles in different samples. (a) Au–SiO_2, Au-n-Si and Au-p-Si, (b) Au–SiO_2 and Au–TiO_2–SiO_2, (c) Au-n-Si and Au–TiO_2-n-Si, and (d) Au-p-Si and Au–TiO_2-p-Si.
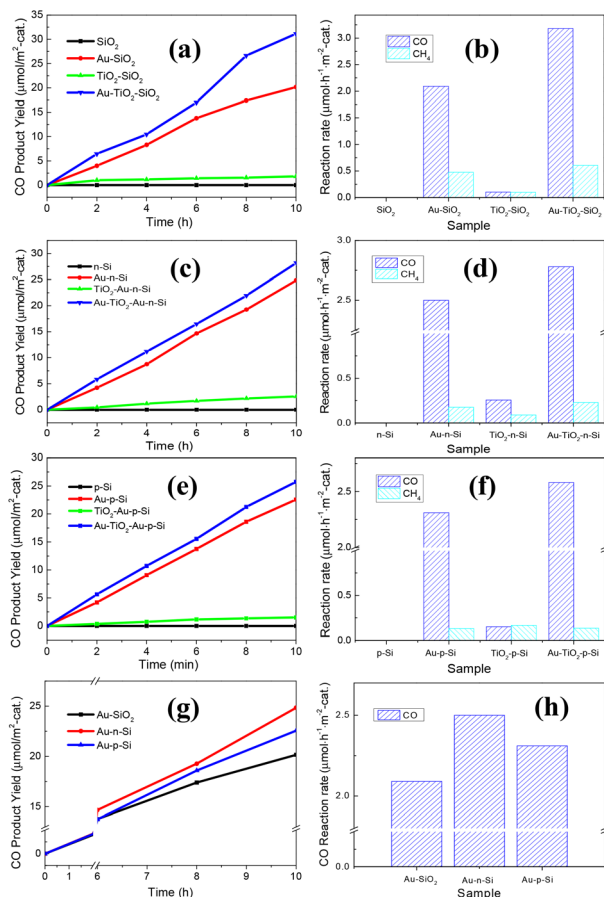
Fig. 8 Products of the photocatalytic CO_2 reduction of different samples. (a) CO product yields of different samples change with time on the SiO_2 substrate. (b) The reaction rates of CO and CH_4 of different samples change with time on the SiO_2 substrate. (c) CO product yields of different samples change with time on the n-Si substrate. (d) The reaction rates of CO and CH_4 of different samples change with time on the p-Si substrate. (e) CO product yields of different samples change with time on the n-Si substrate. (f) The reaction rates of CO and CH_4 of different samples change with time on the p-Si substrate. (g) CO reaction rates of Au–SiO_2 and Au-n-Si. (h) CO reaction rates of Au–SiO_2 and Au-p-Si.

nature of TiO_2 and high exciton recombination and reflection of incident light of n-Si. Au–TiO_2-n-Si shows much larger photocurrent than Au-n-Si, implying that it has a greater ability for charge transfer and exhibits a stronger plasmon effect.

4. Discussion

As indicated above, the plasmon effect can have a huge impact on the photocatalytic performance, while the mechanism may vary on a case-by-case basis. The first one to be discussed is the local heating effect, which is only related to the plasmon effect of the metal itself. Here only the blank SiO_2 substrate and Au–SiO_2 are used as the example. The average surface temperature is about 19.31 and 20.37 °C for SiO_2 before and after visible-light irradiation, and it is 19.01 and 20.39 °C for

Au–SiO_2 (Fig. S9†). Thus, the temperature increase upon illumination is too small to be ignored. Accordingly, the local thermal effect is not considered. This is consistent with the literature that the influence of the local heating effect owing to the metallic LSPs on the photocatalytic reaction is almost negligible.[17,30,51] Thus, only the PRE and DET mechanisms are discussed in this work.

It is believed that DET and PRE may exist simultaneously in the photocatalytic CO_2RR. Since Au–SiO_2 exhibits stronger plasmon excitation (*i.e.*, stronger PRE effect) than Au–TiO_2–SiO_2 and Au-n-Si (Au-p-Si), the DET mechanism overwhelms PRE for Au–TiO_2–SiO_2 and Au-n-Si (Au-p-Si) considering that Au–SiO_2 has lower catalytic activity than Au–TiO_2–SiO_2 and Au-n-Si (Au-p-Si). In addition, it is noted that Au-n-Si (Au-p-Si) has a weaker PRE effect than Au–TiO_2-n-Si (Au–TiO_2-p-Si). Although this may explain why the catalytic activity of Au-n-Si (Au-p-Si) is lower than that of Au–TiO_2-n-Si (Au–TiO_2-p-Si), it is hard to distinguish which one (PRE or DET) is dominant in the enhanced catalytic activity, as Au-n-Si (Au-p-Si) also shows a weaker DET effect than Au–TiO_2-n-Si (Au–TiO_2-p-Si) based on the band structures discussed below.

The reactive sites and related mechanism of photocatalytic CO_2RR can be further explained according to the alignment of energy levels of different materials, as shown in Fig. S10.† The detailed mechanism is depicted in Fig. 9. Under the visible light irradiation, SiO_2 (Fig. 9(a)) and TiO_2–SiO_2 (Fig. 9(c)) do not exhibit catalytic activity due to their wide bandgap characteristics. The occurrence of CO_2RR over Au–SiO_2 is mainly due
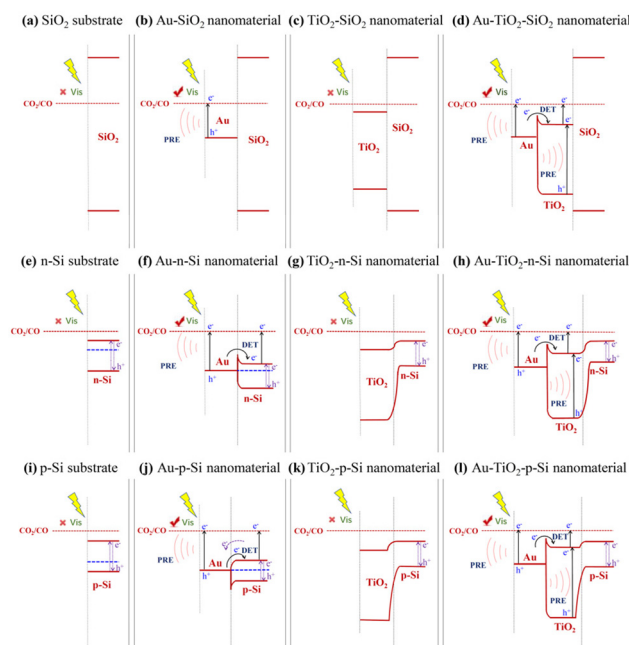

Fig. 9 Schematic diagrams showing the photocatalytic CO_2RR mechanism under visible-light illumination over different samples of (a) SiO_2, (b) Au–SiO_2, (c) TiO_2–SiO_2, (d) Au–TiO_2–SiO_2, (e) n-Si, (f) Au-n-Si, (g) TiO_2-n-Si, (h) Au–TiO_2-n-Si, (i) p-Si, (j) Au-p-Si, (k) TiO_2-p-Si, and (l) Au–TiO_2-p-Si.

to the PRE mechanism (Fig. 9(b)), for which both oxidation and reduction reactions occur on the Au surface (*i.e.*, Au acts as the catalyst), which agrees with a previous report.[13] For Au–TiO_2–SiO_2, because of the weaker PRE effect but higher catalytic activity compared with Au–SiO_2, the photocatalytic reactions not only take place on the Au surface, but also occur on TiO_2. Au serves as the catalyst in the former and as the co-catalyst in the latter. However, as discussed above, the catalytic reactions occur mainly *via* the DET mechanism, and the hot electrons produced in the Au particles due to the plasmon effect transfer to the conduction band of TiO_2. Hence, the reduction reactions leading to the conversion of CO_2 to CO occur on the surface of TiO_2, and the oxidation reactions of H_2O into O_2 take place on the Au surface. In this case, the Au/TiO_2 heterojunction acts as the catalyst.

It is noted that no catalytic products can be observed over both n-Si (Fig. 9(e)) and p-Si (Fig. 9(i)). This is mainly due to the exciton recombination of the narrow bandgap and specular reflection of the polished Si surface. TiO_2-n-Si (Fig. 9(g)) and TiO_2-p-Si (Fig. 9(k)) exhibit very weak catalytic activity because of the existence of oxygen vacancies in TiO_2. The CO_2RR over Au-n-Si (Fig. 9(f)) and Au-p-Si (Fig. 9(j)) arises from the PRE effect of Au particles and charge transfer at the interface of Au and Si, leading to the superior catalytic activity to Au–SiO_2. Thus, the oxidation and reduction reactions take place on the Au surface in terms of the PRE mechanism, *i.e.*, Au serves as the catalyst; while the reduction reaction mainly happens on the Si surface in light of the DET mechanism, and the oxidation reaction occurs on the Au surface, *i.e.*, Au/Si heterojunction acts as the catalyst.

For Au–TiO_2-n-Si (Fig. 9(h)) and TiO_2-p-Si (Fig. 9(l)), due to the stronger PRE effect compared with Au-n-Si and Au-p-Si, the photocatalytic oxidation and reduction reactions not only occur on the Au surface, but also on TiO_2. In addition, Au/TiO_2 has a stronger DET effect than Au/Si, resulting in enhanced catalytic activity owing to the efficient transfer of electrons from Au to the conduction band of TiO_2. Meanwhile, the photogenerated electrons in Si can transfer to TiO_2 and the holes generated in TiO_2 will transfer to Si, which can promote the photocatalytic reactions too. Therefore, the catalytic efficiency of Au–TiO_2-n-Si (Au–TiO_2-p-Si) is higher than that of Au-n-Si (Au-p-Si), which is also related to the fact that TiO_2 exhibits better separation of charge carriers (*i.e.*, less recombination) due to its larger bandgap compared to Si. Accordingly, Au–TiO_2-n-Si (Au–TiO_2-p-Si) acts as the catalyst. In addition, the major difference between the samples using p-Si and n-Si as the substrates is that the hot electrons transferred from Au to the conduction band of p-Si can migrate back to Au again. This may explain why the catalytic activity of samples with the n-Si substrate is slightly higher than their counterparts with the p-Si substrate.

5. Conclusions

In summary, Au particles have been deposited on various solid supports. The results of the optical refractive index and extinction coefficient, Raman spectra and reflection coefficient indicate that the PRE effect caused by the Au plasmon for Au–SiO_2 is stronger than that of Au–TiO_2–SiO_2 and Au-n-Si (Au-p-Si) in the visible light range, while Au-n-Si (Au-p-Si) is weaker than Au–TiO_2-n-Si (Au–TiO_2-p-Si). The ELF of plasmon for Au–SiO_2 is lower than that of Au–TiO_2–SiO_2 and Au-n-Si (Au-p-Si) in the visible light, while Au-n-Si (Au-p-Si) is larger than Au–TiO_2-n-Si (Au–TiO_2-p-Si). The experimental results can be verified by FDTD simulations. The Au/TiO_2 heterojunction exhibits stronger charge transfer for the photocatalytic CO_2RR than the Au/Si heterojunction. The catalytic activity of Au-n-Si (Au-p-Si) is lower than that of Au–TiO_2-n-Si (Au–TiO_2-p-Si), and Au–SiO_2 is lower than Au–TiO_2–SiO_2 and Au-n-Si (Au-p-Si), implying that the DET mechanism is dominant over the PRE. The mechanism of the photocatalytic CO_2RR under visible-light irradiation over various samples has been proposed based on the optical results and alignment of energy levels. The results indicate that the PRE effect can be valid for any material systems if there is a suitable plasmonic metal. Meanwhile, the DET effect is more feasible for a system in which the metal directly contacts with a semiconductor and the DET effect is stronger than PRE effect. We envision that this work can provide useful information toward understanding the mechanism of plasmon photocatalytic reactions in CO_2 reduction, and facilitate the development of novel plasmon-mediated catalytic systems.

Conflicts of interest

There are no conflicts to declare.

Acknowledgements

References

1 M. Halmann, *Nature*, 1978, **275**, 115–116.
2 T. Inoue, A. Fujishima, S. Konishi and K. Honda, *Nature*, 1979, **277**, 637–638.
3 Y. Zhang, L. Yan, M. Guan, D. Chen, Z. Xu, H. Guo, S. Hu, S. Zhang, X. Liu, Z. Guo, S. Li and S. Meng, *Adv. Sci.*, 2022, **9**, 2102978.
4 R. G. Ciocarlan, N. Blommaerts, S. Lenaerts, P. Cool and S. W. Verbruggen, *ChemSusChem*, 2023, **16**, e202201647.
5 J. Zhang, B. Guan, X. Wu, Y. Chen, J. Guo, Z. Ma, S. Bao, X. Jiang, L. Chen, K. Shu, H. Dang, Z. Guo, Z. Li and Z. Huang, *Catal. Sci. Technol.*, 2023, **13**, 1932–1975.
6 X. Wan, Y. Gao, M. Eshete, M. Hu, R. Pan, H. Wang, L. Liu, J. Liu, J. Jiang, S. Brovelli and J. Zhang, *Nano Energy*, 2022, **98**, 107217.
7 Y. Fu, D. Sun, Y. Chen, R. Huang, Z. Ding, X. Fu and Z. Li, *Angew. Chem.*, 2012, **124**, 3420–3423.

8 M. J. Wu, M. M. Li, Y. J. Wang, X. H. Zhang and T. He, *ACS Appl. Energy Mater.*, 2023, **8**, 5558–5566.

9 J. Yu, J. Low, W. Xiao, P. Zhou and M. Jaroniec, *J. Am. Chem. Soc.*, 2014, **136**, 8839–8842.

10 L. Zhang, W. Wang, D. Jiang, E. Gao and S. Sun, *Nano Res.*, 2015, **8**, 821–831.

11 G. Gao, Y. Jiao, E. R. Waclawik and A. Du, *J. Am. Chem. Soc.*, 2016, **138**, 6292–6297.

12 M. Rahaman, V. Andrei, D. Wright, E. Lam, C. Pornrungroj, S. Bhattacharjee, C. M. Pichler, H. F. Greer, J. J. Baumberg and E. Reisner, *Nat. Energy*, 2023, **8**, 629–638.

13 P. Wang, B. Huang, Y. Dai and M. H. Whangbo, *Phys. Chem. Chem. Phys.*, 2012, **14**, 9813–9825.

14 S. Guo, Z. Tang, Y. Du, T. Liu, T. Ouyang and Z. Liu, *Appl. Catal., B*, 2023, **321**, 122035.

15 S. Huang, F. Feng, R. Huang, T. Ouyang, J. Liu and Z. Liu, *Adv. Mater.*, 2022, **34**, 2208438.

16 T. Ouyang, Y. Ye, C. Tan, S. Guo, S. Huang, R. Zhao, S. Zhao and Z. Liu, *J. Phys. Chem. Lett.*, 2022, **13**, 6867–6874.

17 W. Hou, W. H. Hung, P. Pavaskar, A. Goeppert, M. Aykol and S. B. Cronin, *ACS Catal.*, 2011, **1**, 929–936.

18 Y. L. Li, Y. Liu, H. Y. Mu, R. H. Liu, Y. J. Hao, X. J. Wang, D. Hildebrandt, X. Y. Liu and F. T. Li, *Nanoscale*, 2021, **13**, 2585–2592.

19 N. Q. Wu, *Nanoscale*, 2018, **10**, 2679–2696.

20 Q. Kang, T. Wang, P. Li, L. Liu, K. Chang, M. Li and J. Ye, *Angew. Chem.*, 2015, **127**, 855–859.

21 F. Wang, Z. Lu, H. Guo, G. Zhang, Y. Li, Y. Hu, W. Jiang and G. Liu, *Chem. – Eur. J.*, 2023, **29**, e202202716.

22 S. K. Cushing, J. Li, F. Meng, T. R. Senty, S. Suri, M. Zhi, M. Li, A. D. Bristow and N. Wu, *J. Am. Chem. Soc.*, 2012, **134**, 15033–15041.

23 W. Tu, Y. Zhou, H. Li, P. Li and Z. Zou, *Nanoscale*, 2015, **7**, 14232–14236.

24 K. M. Choi, D. Kim, B. Rungtaweevoranit, C. A. Trickett, J. T. D. Barmanbek, A. S. Alshammari, P. Yang and O. M. Yaghi, *J. Am. Chem. Soc.*, 2017, **139**, 356–362.

25 A. Furube, L. Du, K. Hara, R. Katoh and M. Tachiya, *J. Am. Chem. Soc.*, 2007, **129**, 14852–14853.

26 J. Li, S. K. Cushing, J. Bright, F. Meng, T. R. Senty, P. Zheng, A. D. Bristow and N. Wu, *ACS Catal.*, 2012, **3**, 47–51.

27 Y. Tang, Z. Jiang, G. Xing, A. Li, P. D. Kanhere, Y. Zhang, T. C. Sum, S. Li, X. Chen, Z. Dong and Z. Chen, *Adv. Funct. Mater.*, 2013, **23**, 2932–2940.

28 Z. Zheng, T. Tachikawa and T. Majima, *J. Am. Chem. Soc.*, 2015, **137**, 948–957.

29 R. Shi, Y. Cao, Y. Bao, Y. Zhao, G. I. N. Waterhouse, Z. Fang, L. Wu, C. Tong, Y. Yin and T. Zhang, *Adv. Mater.*, 2017, **27**, 1700803.

30 P. Christopher, D. B. Ingram and S. Linic, *J. Phys. Chem. C*, 2010, **114**, 9173–9177.

31 S. Mukherjee, L. Zhou, A. M. Goodman, N. Large, C. Ayala-Orozco, Y. Zhang, P. Nordlander and N. J. Halas, *J. Am. Chem. Soc.*, 2013, **136**, 64–67.

32 K. Wu, W. E. Rodríguez-Córdoba, Y. Yang and T. Lian, *Nano Lett.*, 2013, **13**, 5255–5263.

33 U. Banin, Y. Ben-Shahar and K. Vinokurov, *Chem. Mater.*, 2013, **26**, 97–110.

34 K. Wu, J. Chen, J. R. McBride and T. Lian, *Science*, 2015, **349**, 632–635.

35 S. Mukherjee, L. Zhou, A. M. Goodman, N. Large, C. Ayala-Orozco, Y. Zhang, P. Nordlander and N. J. Halas, *J. Am. Chem. Soc.*, 2013, **136**, 64–67.

36 X. Zhang, X. Li, D. Zhang, N. Q. Su, W. Yang, H. O. Everitt and J. Liu, *Nat. Commun.*, 2017, **8**, 14542.

37 Y. Zhang, X. Han, R. Liu, Y. Liu, H. Huang, J. Zhang, H. Yu and Z. Kang, *J. Phys. Chem. C*, 2012, **116**, 20363–20367.

38 Y. Qu and X. Duan, *Chem. Soc. Rev.*, 2013, **42**, 2568–2580.

39 M. W. Knight, H. Sobhani, P. Nordlander and N. J. Halas, *Science*, 2011, **332**, 702–704.

40 J. Y. Park, H. Lee, J. R. Renzas, Y. Zhang and G. A. Somorjai, *Nano Lett.*, 2008, **8**, 2388–2392.

41 C. Q. Lai, W. Zheng, W. K. Choi and C. V. Thompson, *Nanoscale*, 2015, **7**, 11123–11134.

42 X. H. Wang, J. G. Li, H. Kamiyama, M. Katada, N. Ohashi, Y. Moriyoshi and T. Ishigaki, *J. Am. Chem. Soc.*, 2005, **127**, 10982–10990.

43 M. G. Blaber, A. I. Henry, J. M. Bingham, G. C. Schatz and R. P. Van Duyne, *J. Phys. Chem. C*, 2011, **116**, 393–403.

44 A. Konrad, A. M. Kern, M. Brecht and A. J. Meixner, *Nano Lett.*, 2015, **15**, 4423–4428.

45 A. S. Kirakosyan, M. I. Stockman and T. V. Shahbazyan, *Phys. Rev. B*, 2016, **94**, 155429.

46 M. A. Noginov, G. Zhu and V. I. Gavrilenko, *Opt. Express*, 2007, **15**, 15648–15655.

47 N. Kim, S. Kim, M. Choi, H. H. Park, N. H. Kim, S. Y. Park, K. M. Byun and S. Y. Lee, *Sens. Actuators, B*, 2018, **258**, 18–24.

48 Z. Li, Y. Xiao, Y. Gong, Z. Wang, Y. Kang, S. Zu, P. M. Ajayan, P. Nordlander and Z. Fang, *ACS Nano*, 2015, **9**, 10158–10164.

49 S. C. Liou, C. S. Shie, C. H. Chen, R. Breitwieser, W. W. Pai, G. Y. Guo and M. W. Chu, *Phys. Rev. B*, 2015, **91**, 045418.

50 S. N. Habisreutinger, L. Schmidt-Mende and J. K. Stolarczyk, *Angew. Chem., Int. Ed.*, 2013, **52**, 7372–7408.

51 Z. Liu, W. Hou, P. Pavaskar, M. Aykol and S. B. Cronin, *Nano Lett.*, 2011, **11**, 1111–1116.